

# GOODS-*Herschel*: evidence for a UV extinction bump in galaxies at $z > 1$

V. Buat<sup>1</sup>, E. Giovannoli<sup>1</sup>, S. Heinis<sup>1</sup>, V. Charmandaris<sup>2,3,4</sup>, D. Coia<sup>5</sup>, E. Daddi<sup>6</sup>, M. Dickinson<sup>7</sup>, D. Elbaz<sup>6</sup>, H.S. Hwang<sup>6</sup>, G. Morrison<sup>8,9</sup>, K. Dasyra<sup>6,4</sup>, H. Aussel<sup>6</sup>, B. Altieri<sup>5</sup>, H. Dannerbauer<sup>6</sup>, J. Kartaltepe<sup>7</sup>, R. Leiton<sup>6</sup>, G. Magdis<sup>6</sup>, B. Magnelli<sup>10</sup>, and P. Popesso<sup>10</sup>

<sup>1</sup> Laboratoire d'Astrophysique de Marseille, OAMP, Université Aix-marseille, CNRS, 38 rue Frédéric Joliot-Curie, 13388 Marseille cedex 13, France

e-mail: veronique.buat@oamp.fr

<sup>2</sup> University of Crete, Department of Physics and Institute of Theoretical & Computational Physics, GR-71003 Heraklion, Greece

<sup>3</sup> IESL/Foundation for Research & Technology-Hellas, GR-71110 Heraklion, Greece

<sup>4</sup> Chercheur Associé, Observatoire de Paris, LERMA (CNRS:UMR8112), 61 Av. de l'Observatoire, F-75014, Paris, France

<sup>5</sup> Herschel Science Operation Centre, ESAC, ESA, PO Box 78, 28691 Villanueva de la Cañada, Madrid, Spain

<sup>6</sup> Laboratoire AIM-Paris-Saclay, CEA/DSM/Irfu - CNRS - Université Paris Diderot, CE-Saclay, F-91191 Gif-sur-Yvette, France

<sup>7</sup> National Optical Astronomy Observatory, 950 North Cherry Avenue, Tucson, AZ 85719, USA

<sup>8</sup> Institute for Astronomy, University of Hawaii, Honolulu, HI, 96822, USA

<sup>9</sup> Canada-France-Hawaii telescope, Kamuela, HI, 96743, USA

<sup>10</sup> Max-Planck-Institut für Extraterrestrische Physik (MPE), Postfach 1312, 85741, Garching, Germany

## ABSTRACT

**Context.** Dust attenuation curves in external galaxies are useful to study their dust properties as well as to interpret their intrinsic spectral energy distributions. These functions are not very well known in the UV range either at low or high redshift. In particular the presence or absence of a UV bump at 2175 Å remains an open issue which has consequences on the interpretation of broad band colours of galaxies involving the UV range.

**Aims.** We want to study the dust attenuation curve in the UV range at  $z > 1$  where the UV is redshifted into the visible, and with *Herschel* data to constrain dust emission and a global dust attenuation. In particular we will search for the presence of a UV bump and the related implications on dust attenuation determinations.

**Methods.** We use deep photometric data of the Chandra Deep Field South obtained with intermediate and broad band filters by the MUSYC project to sample the UV rest-frame of galaxies with  $1 < z < 2$ . *Herschel*/PACS and *Spitzer*/MIPS data are used to measure the dust emission. 30 galaxies were selected with high S/N in all bands. Their SEDs from the UV to the far-IR are fitted using the CIGALE code and the characteristics of the dust attenuation curve are obtained as Bayesian outputs of the SED fitting process.

**Results.** The mean dust attenuation curve we derive exhibits a significant UV bump at 2175 Å whose amplitude corresponds to 35% (76 %) that of the Milky Way (Large Magellanic Cloud: LMC2 supershell) extinction curve. An analytical expression of the average attenuation curve ( $A(\lambda)/A_V$ ) is given, it is found slightly steeper than the Calzetti et al. one, although at a  $1\sigma$  level. Our galaxy sample is used to study the derivation of the slopes of the UV continuum from broad band colours, including the rest-frame GALEX *FUV* – *NUV* colour. Systematic errors induced by the presence of the bump are quantified. We compare dust attenuation factors measured with CIGALE to the slope of the UV continuum and find that there is a large scatter around the relation valid for local starbursts ( $\sim 0.7$  mag). The uncertainties on the determination of the UV slope lead to an extra systematic error of the order of 0.3 to 0.7 mag on dust attenuation when a filter overlaps the UV bump.

**Conclusions.**

**Key words.** Galaxies: high-redshift-Galaxies: ISM-Ultraviolet : galaxies-Infrared: galaxies-ISM: dust, extinction

## 1. Introduction

Stellar light in galaxies is absorbed and scattered by the interstellar medium, because of the presence of dust grains. On a galaxy scale, the process is usually quantified by the introduction of an average attenuation function which reflects the combined effects of absorption and scattering in a complex geometry.

The most important feature in the extinction curves of the Milky Way (MW) and Large Magellanic Cloud (LMC) is the so called UV bump, a strong absorption feature at 2175 Å which is not observed in the Small Magellanic Cloud (SMC) bar, although a line of sight through the SMC wing exhibits an extinction curve

with a strong UV bump (Li & Draine, 2002; Cartledge et al., 2005). The exact origin of this feature is still under discussion (e.g. Draine, 1989; Xiang et al., 2011, and references therein). When dealing with average attenuation curves, the search for a bump is complicated by the effects of scattering or geometry (Inoue et al., 2006; Noll et al., 2007; Panuzzo et al., 2007) which may affect the amplitude of the resulting bump in an average attenuation curve even when assuming a local Milky Way like extinction curve.

The best way to study UV bumps in external galaxies is to perform UV rest-frame spectroscopy: Calzetti et al. (1994) deduced the net attenuation curves of local starburst galaxies by comparing the UV spectra of dusty and dust-free spectra of local starbursts: they did not find any bump. Conversely, Noll et al. (2005,

2009a) observed a significant 2175 Å absorption feature in the spectra of star forming galaxies at  $z \sim 2$  consistent with an extinction curve intermediate between the SMC and LMC ones.

The 2175 Å feature has also been detected in the spectral energy distribution of some distant galaxies hosting gamma-ray bursts (Liang & Li, 2009, 2010), the extinction curves are found to display a large diversity of shapes (Liang & Li, 2009, 2010; Zafar et al., 2011, and references therein). We also refer to Xiang et al. (2011) for an extensive review on the detection of the UV bump in Galactic and extragalactic interstellar medium.

Broad band colours are also used to search for evidence of a UV bump. From an analysis of the observed B-R colours of galaxies at  $z \sim 1$  Conroy (2010) disfavours the presence of UV bumps as strong as that in the Milky Way whereas Burgarella et al. (2005) analysed the broad bands SEDs of nearby galaxies observed by GALEX and IRAS and conclude to the presence of a bump in the attenuation curve of these galaxies. In all cases, the use of broad band colours which overlap the bump makes difficult to disentangle the effects of a dust extinction curve with or without a bump, of dust/stars geometry and of various star formation histories (Inoue et al., 2006; Panuzzo et al., 2007; Johnson et al., 2007a,b; Buat et al., 2011) leading to contradicting conclusions on the presence of a UV bump in nearby galaxies observed by GALEX and SDSS (Conroy et al., 2010; Johnson et al., 2007a,b).

The presence and characteristics of the UV bump, and far UV rise in the extinction and attenuation curves can provide information on the interstellar medium properties (Noll et al., 2009a). Beyond the studies of the interstellar medium, a reliable attenuation curve in the UV range is very useful to derive star formation rates in galaxies since the UV emission is commonly used as a star formation tracer. For example, Wijesinghe et al. (2010) compared star formation rates deduced from luminosities measured in the GALEX bands and the H $\alpha$  and [OII] emission lines and concluded that they must remove the 2175 Å feature from the attenuation curve to obtain the best agreement between the different SFR estimators. The attenuation curve of Calzetti et al. (2000) is commonly used, especially in high- $z$  studies and does not include a bump: if such a bump is present, omitting it leads to incorrect dust attenuation corrections (Ilbert et al., 2009).

The global amount of dust attenuation is robustly estimated by comparing dust and stellar emission, through the  $L_{\text{IR}}/L_{\text{UV}}$  ratio. When IR data are not available the shape of the UV continuum ( $< 3000$  Å) has been proposed as a proxy to measure the amount of attenuation. Calzetti et al. (1994) showed that the UV continuum of local starburst galaxies can be fit by a power law ( $f_{\lambda}(\text{erg cm}^{-2}\text{s}^{-1}\text{Å}^{-1}) \propto \lambda^{\beta}$ ) for  $\lambda > 1200$  Å. They calculated  $\beta$  by defining 10 windows in the IUE spectra of their galaxies avoiding the 2175 Å feature. Meurer et al. (1999) found a relation between  $\beta$  and the amount of dust attenuation measured by  $L_{\text{IR}}/L_{\text{UV}}$ . This local starburst relation is widely used to estimate dust attenuation in high redshift galaxies using a broad band colour in the UV rest-frame of the galaxies as a proxy of  $\beta$  (e.g. Burgarella et al., 2007; Elbaz et al., 2007; Daddi et al., 2007; Reddy et al., 2008). If a bump is present in the dust attenuation curve, one must be cautious by choosing broad band filters which do not overlap the bump in order to estimate reliable slopes outside the wavelength range affected by the bump, as was done to derive the Meurer et al. (1999) relation. This has been illustrated by studies of the local universe based on GALEX FUV and NUV data: the NUV band largely overlaps the UV bump and the FUV-NUV colour is found to be sensitive to the presence or absence of this feature as well as to the recent star formation his-

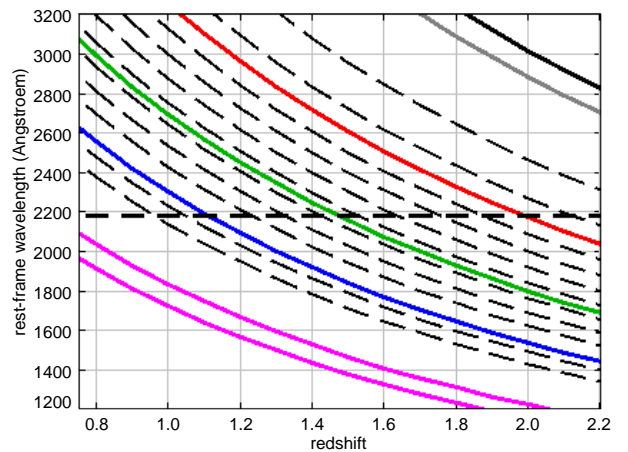


Fig. 1: Rest-frame ultraviolet wavelengths sampled with our dataset as a function of redshift. The solid curves correspond to broad band filters (from bottom left corner to top right corner: U, U38, B, V, R, I and z) and the dashed curves to intermediate-band filters (from bottom left corner to top right corner: IA-427, 445, 484, 505, 527, 550, 574, 598, 624, 651 (coincident with the red solid curve for the R-band), 679 and 738. The FWHM of the intermediate filters varies from 20 to 34 nm. The horizontal dotted line corresponds to 2175 Å, the central wavelength of the expected bump.

tory (Panuzzo et al., 2007; Inoue et al., 2006).

In this paper we take advantage of the availability of high quality deep optical data obtained through intermediate-band filters in the Chandra Deep Field South (CDFs) to sample the rest-frame UV of galaxies at high redshift. These data are combined with the *Herschel* observations of the CDFs field as part of the open time key program GOODS-*Herschel* project (P.I. D. Elbaz). The galaxies detected in the far-IR are expected to experience a substantial extinction, which helps to detect the imprint of the bump in their SED. The combination of UV and IR data will allow us to compare the properties of the UV continuum to the dust attenuation at work in these objects. In a similar vein, Ilbert et al. (2009) used broad and intermediate band filters to derive photometric redshifts in the COSMOS field and found that a UV bump is necessary to explain the UV rest-frame fluxes of some starburst galaxies but they did not discuss the amplitude of the bump and dust attenuation in these galaxies.

The construction of the sample is explained in section 2. We want to use only sources detected with high signal to noise ratio (SNR) in a large number of filters which sample well the rest-frame UV wavelength region affected by the bump. This criterion leads to a redshift selection between 0.95 and 2.2. The dust attenuation curve as well as the amount of dust obscuration is constrained by fitting the whole SEDs of the galaxies with the CIGALE code, which is described in section 3. Section 4 is devoted to the results about the presence of the UV bump and section 5 to the consequences on the determination of the slope of the UV continuum and dust attenuation in galaxies. The conclusions are presented in section 6.

## 2. Selection of the sample

As part of the GOODS-*Herschel* key program (Elbaz et al., 2011), the *Herschel* Space Observatory (Pilbratt et al., 2010) surveyed a small area of the Great Observatories Origins Deep Survey Southern field (GOODS-S):  $10' \times 10'$  centered on the

Table 1: Galaxy sample

N	RA (2000) deg	DEC (2000) deg	z	$\log(L_{\text{IR}})$ $L_{\odot}$	$A_{\text{UV}}$ mag	$E_b$	$err_{E_b}$	$\gamma$ $\text{\AA}$	$err_{\gamma}$ $\text{\AA}$	$\delta$	$err_{\delta}$	$\chi^2_{\text{min}}$
1	03:32:36.19	-27:42:58.2	0.967	11.45	1.14	0.98	0.67	339.32	107.00	0.09	0.03	3.16
2	03:32:20.72	-27:44:53.7	0.969	11.50	2.80	1.74	0.31	361.66	102.58	-0.30	0.00	2.69
3	03:32:16.45	-27:44:48.7	0.976	11.49	2.98	1.15	0.61	348.02	107.33	0.03	0.07	2.63
4	03:32:31.80	-27:49:58.4	0.98 <sup>2</sup>	11.49	2.89	1.18	0.54	360.33	107.93	-0.16	0.09	1.43
5	03:32:42.28	-27:47:46.1	0.998	11.43	1.98	1.68	0.34	376.98	101.85	-0.20	0.12	2.31
6	03:32:37.39	-27:44:07.0	1.018	11.28	3.90	1.51	0.46	350.17	106.16	-0.24	0.06	1.76
7	03:32:06.43	-27:47:28.7	1.021	11.69	3.75	1.25	0.54	370.61	106.19	-0.29	0.03	2.30
8 <sup>1</sup>	03:32:15.78	-27:46:30.2	1.023	11.35	1.68	1.05	0.65	347.67	107.83	-0.21	0.05	3.72
9	03:32:36.02	-27:44:23.8	1.038	11.34	1.98	1.55	0.45	351.24	106.58	-0.02	0.05	1.65
10	03:32:10.58	-27:47:06.1	1.045	11.42	2.83	0.95	0.62	352.28	108.69	-0.10	0.09	1.24
11	03:32:28.98	-27:49:08.2	1.094	11.59	2.01	1.63	0.43	375.24	102.58	-0.29	0.02	5.58
12	03:32:39.87	-27:47:15.0	1.095	11.43	1.93	1.79	0.29	400.42	92.73	-0.27	0.07	2.25
13	03:32:25.86	-27:50:19.6	1.095	11.52	2.40	1.42	0.52	355.97	106.19	-0.16	0.06	2.30
14 <sup>1</sup>	03:32:17.18	-27:52:20.5	1.097	12.09	5.61	1.03	0.39	368.57	104.51	-0.30	0.02	4.56
15	03:32:34.85	-27:46:40.5	1.099	11.46	4.19	1.61	0.43	373.69	102.00	-0.18	0.08	1.08
16	03:32:34.63	-27:53:24.5	1.107	11.61	2.47	1.04	0.64	344.75	107.87	-0.03	0.10	1.12
17 <sup>1</sup>	03:32:29.97	-27:45:29.8	1.209	12.07	1.13	0.87	0.67	328.56	106.76	0.08	0.04	15.92
18	03:32:43.48	-27:45:56.5	1.220	11.45	2.54	1.35	0.55	336.36	105.68	-0.21	0.06	2.70
19	03:32:47.17	-27:51:06.1	1.224	11.82	4.66	1.10	0.50	337.70	107.00	-0.29	0.03	1.22
20 <sup>1</sup>	03:32:35.97	-27:48:50.4	1.309	11.54	1.24	0.87	0.67	337.88	107.68	0.02	0.07	2.70
21 <sup>1</sup>	03:32:29.93	-27:43:01.0	1.37 <sup>2</sup>	12.12	4.29	1.62	0.32	408.06	89.38	0.01	0.06	1.71
22 <sup>1</sup>	03:32:28.79	-27:47:55.6	1.383	11.69	4.02	0.66	0.47	331.44	107.91	-0.21	0.07	3.36
23	03:32:34.03	-27:50:28.8	1.384	11.82	3.32	1.45	0.38	369.56	102.64	0.08	0.04	2.50
24	03:32:41.33	-27:45:38.2	1.52 <sup>2</sup>	11.91	3.69	1.30	0.51	332.05	107.31	-0.20	0.08	1.53
25 <sup>1</sup>	03:32:37.76	-27:52:12.3	1.609	12.33	4.63	1.03	0.51	333.88	111.60	-0.04	0.05	6.39
26	03:32:37.71	-27:50:00.4	1.619	12.43	5.21	0.94	0.36	352.65	105.73	-0.09	0.07	2.88
27	03:32:17.82	-27:46:39.7	1.956	11.93	2.85	0.83	0.60	368.08	107.77	0.01	0.08	1.69
28	03:32:41.77	-27:46:56.4	1.994	12.00	3.32	1.03	0.50	351.00	107.88	0.02	0.09	2.85
29	03:32:40.05	-27:47:55.4	1.997	12.40	3.79	1.39	0.40	328.89	103.03	-0.13	0.10	2.30
30	03:32:40.75	-27:49:26.1	2.130	12.12	3.02	1.33	0.53	350.01	107.06	-0.08	0.11	1.41

**Notes.** IR luminosities( $\log(L_{\text{IR}})$ ), dust attenuation ( $A_{\text{UV}}$ ) and parameters relative to the attenuation curve (the amplitude and width of the UV bump,  $E_b$  and  $\gamma$ , and the steepness of the curve,  $\delta$ ) and their corresponding errors are obtained from the Bayesian analysis performed with CIGALE.

<sup>(1)</sup> X-ray emitter

<sup>(2)</sup> No spectroscopic redshift, the photometric redshift is used.

CDFS were observed at 100 and 160  $\mu\text{m}$  over 264 hours by the PACS instrument (Poglitsch et al., 2010). Source extraction on the PACS images was performed at the prior position of *Spitzer* 24  $\mu\text{m}$  sources as described in Elbaz et al. (2011).

Cardamone et al. (2010, the MUSYC project) compiled a uniform catalog of optical and infrared photometry for sources in GOODS-S, incorporating the GOODS *Spitzer* IRAC and MIPS data (Dickinson et al., 2003). In particular, they used deep intermediate-band imaging from the Subaru telescope to provide photometry with finer wavelength sampling than is possible from standard broad band data. This was done in part to enable more accurate photometric redshifts, but for our purposes here it provides a valuable means of tracing the detailed shape of the UV rest-frame spectrum and to look for the presence of a UV absorption bump.

We start with the GOODS-*Herschel* catalogue of 533 sources detected at 100  $\mu\text{m}$ , and identify 325 sources with a SNR (flux over error) at 100  $\mu\text{m}$  larger than 5. We further restrict the sample to the 235 sources also detected at 160  $\mu\text{m}$  with a SNR  $> 3$  and we cross-correlate them with the MUSYC catalogue of 84402 sources with photometric redshifts. The tolerance radius between IRAC and optical coordinates is taken to be 2 arcsec, it results in a sample of 219 sources cross-matched. Total fluxes in optical and *Spitzer* bands are computed from aperture fluxes as described in Cardamone et al. (2010).

Before selecting sources according to their redshift we must

choose the bands we will use: the redshift range will be selected to ensure a good sampling of the UV range. All the optical broad bands of the MUSYC survey are considered (U, U38, B, V, R, I, z) and J, H, K bands are added when available. We also add data from intermediate band filters whose  $5\sigma$  depth is fainter than 25 ABmag (table 2 of Cardamone et al. (2010)). Practically we use IA-427, 445, 484, 505, 527, 550, 574, 598, 624, 651, 679 and 738. Figure 1 illustrates the rest-frame wavelengths corresponding to these filters as a function of  $z$ .

In order to ensure a good photometric sampling around the UV bump (2175  $\text{\AA}$ ) we select galaxies with redshifts between 0.95 and 2.2. In this redshift range we have more than 10 photometric bands available in the UV (1300-3000  $\text{\AA}$ ) and a good sampling around 2175  $\text{\AA}$  (Fig.1). 76 galaxies fulfill the redshift condition. To ensure that sources at  $z < 1.6$  have data below rest-frame 1800  $\text{\AA}$ , they must have been detected in the U and U38 filters above  $5\sigma$  (see Table 3 of Cardamone et al. (2010)). This leads us to 39 galaxies all of which are also strongly detected in the other broad bands as well as above  $5\sigma$  in the IA-427 filter. When  $z > 1.6$ , measurements beyond the U filter are sufficient, so we select sources detected with SNR  $> 5$  in the B band, adding an additional constrain of a  $5\sigma$  detection an intermediate filter (IA-427 for  $z < 1.8$  and IA-484 for  $z > 1.8$ ), 13 galaxies are thus added to the selection. At the end we have selected 52 galaxies. As a further check, we retrieve the HST images at the coordinates of these 52 sources using the GOODS cutout service V2.0 provided

by the Multimission Archive at STScI (<http://archive.stsci.edu>). We discard 22 sources with bright neighbours closer than 4 arcsec to the *Herschel* detection and whose IR measurements are uncertain (the FWHM of the PSF at  $100 \mu\text{m}$  is  $6.7$  arcsec). Half of the remaining sample of 30 galaxies has a disk-like morphology, the other half is dominated by compact sources with few interacting-peculiar galaxies while 28 have spectroscopic redshifts. The sample of galaxies is presented in Table 1. The HST images for each target are available as online material. 7 galaxies are identified as X-ray emitters by Cardamone et al. (2008) they are flagged in Table 1.

As described earlier in this section, the present study is based on galaxies strongly detected from the UV to the far-IR, whose rest-frame UV spectrum is sampled by several intermediate-band filters. These highly selective criteria lead to a rather small sample of objects which we will study in detail in this paper in order to derive the parameters of a dust attenuation curve. Our analysis is complementary to other studies at intermediate and high redshifts which are based on larger samples but they lack far-IR data. These studies have concluded that a UV bump must be introduced in the attenuation curve but they were not able to quantify neither the amplitude of the bump nor the modification of the attenuation curve (Ilbert et al., 2009; Kriek et al., 2011)

### 3. SED fitting with CIGALE

SED fitting is performed with the CIGALE code (Code Investigating GALaxy Emission) developed by Noll et al. (2009b). This is a physically-motivated code which derives properties of galaxies by fitting their UV-to-far-IR SEDs. CIGALE combines a UV-optical stellar SED and a dust, IR-emitting component and fully conserves the energetic balance between the dust absorbed stellar emission and its e-emission in IR. We refer to Giovannoli et al. (2010) for details on the use of CIGALE to fit SEDs of actively star forming galaxies observed both in UV and far-IR (rest-frame). In the present work, the sampling of the UV range is very good so we expect to constrain the dust attenuation curve. To model the attenuation by dust, the code uses the attenuation law of Calzetti et al. (2000) as a baseline, and offers the possibility of varying the steepness of this law and adding a bump centered at  $2175 \text{ \AA}$ . We refer to Noll et al. (2009b) for a complete description of the dust attenuation prescription. The dust attenuation is described as:

$$A(\lambda) = \frac{A_V}{4.05} (k'(\lambda) + D_{\lambda_0, \gamma, E_b}(\lambda)) \left( \frac{\lambda}{\lambda_V} \right)^\delta \quad (1)$$

where  $\lambda_V = 5500 \text{ \AA}$ ,  $k'(\lambda)$  comes from Calzetti et al. (2000) (Eq.4) and  $D_{\lambda_0, \gamma, E_b}(\lambda)$ , the Lorentzian-like Drude profile commonly used to describe the UV bump (Fitzpatrick & Massa, 1990; Noll et al., 2009a) is defined as:

$$D_{\lambda_0, \gamma, E_b} = \frac{E_b \lambda^2 \gamma^2}{(\lambda^2 - \lambda_0^2)^2 + \lambda^2 \gamma^2} \quad (2)$$

The peak amplitude above the continuum, full width half maximum (FWHM) and central wavelength of the bump ( $E_b$ ,  $\gamma$  and  $\lambda_0$ ) are free parameters of the code<sup>1</sup>. There is no indication for variations of the central wavelength of the bump either in the Milky Way or in external galaxies (Noll et al., 2009a, and references therein), therefore we fix the central wavelength of the

<sup>1</sup>  $E_b$  and  $\gamma$  are related to the original parameters  $c_3$  and  $\gamma_{\text{FM}}$  introduced by Fitzpatrick & Massa (1990):  $E_b = c_3/\gamma_{\text{FM}}^2$  and  $\gamma = \gamma_{\text{FM}} \times \lambda_0^2$

bump  $\lambda_0$  to  $2175 \text{ \AA}$ . The parameter  $\gamma$ , indicating the FWHM, can vary between  $200$  and  $500 \text{ \AA}$  in order to cover the range of values found in previous studies: the FWHM found in the Milky Way is  $437 \text{ \AA}$  (Fitzpatrick & Massa, 2007) while Noll et al. (2009a) found a FWHM of  $274 \text{ \AA}$  for their composite spectrum of galaxies with  $1.5 < z < 2.5$ . After several trade-offs, the amplitude of the bump  $E_b$  is chosen between  $0$  and  $2$ . For comparison the corresponding value for the extinction curve of the Milky Way is  $3.52$  (Fitzpatrick & Massa, 2007),  $1.63$  for the LMC2 supershell (Gordon et al., 2003), and between  $0.5$  and  $1$  for  $z \sim 2$  galaxies (Noll et al., 2009a).

Finally we choose  $\delta$  between  $-0.3$  and  $0.1$ , this range of values is also chosen after several trade-offs, excluding values never chosen by the code.

The stellar population created by CIGALE is the combination of an old, exponentially decreasing, component (starting at the age of the universe at the redshift of the galaxy) and a young burst of constant star formation beginning between  $0.3 \cdot 10^8$  and  $310^8$  years ago. The e-folding rate of the old stellar population is found to be  $2 \pm 0.4$  Gyr. Since the UV emission reaches a stationary state after  $\sim 10^8$  years of constant star formation, the general shape of the UV SEDs analyzed in this work is predominantly modified by the effect of dust attenuation (Calzetti et al., 1994). The attenuation correction is applied to each component. To take into account the different distributions of stars of different ages, we adopt a visual attenuation  $A_V$  for the old stellar component equal to half that used for the young component. The exact value of this reduction factor (called  $f_{\text{att}}$  in the code) is very difficult to constrain even if a value lower than  $1$  is always found (Noll et al., 2009b; Buat et al., 2011). In a first step we ran CIGALE with  $f_{\text{att}}$  as a free parameter with values comprised between  $0$  and  $1$ , we obtained a mean value of  $0.5$  for  $f_{\text{att}}$ . To reduce the computation time we decided to freeze the value of  $f_{\text{att}}$ , after checking that it did not modify the values obtained for the other output parameters of the code.

Dust luminosities,  $\log(L_{\text{IR}})$  between  $8$  and  $1000 \mu\text{m}$ , are computed by fitting Dale & Helou (2002) templates and are linked to the attenuated stellar population models (the stellar luminosity absorbed by the dust is re-emitted in IR). The validity of Dale & Helou (2002) templates to measure total IR luminosities of sources detected by *Herschel* is confirmed by the studies of Elbaz et al. (2010, 2011). Non-thermal sources, not linked to the absorbed stellar population can also contribute to the dust emission. CIGALE includes dust-enshrouded AGNs by adding two PAH-free templates from Siebenmorgen et al. (2004) as described in Buat et al. (2011). These two templates differ by the amount of silicate absorption and their spectral distribution beyond  $20$  microns is similar to the mean template constructed by Mullaney et al. (2011). The spectrum below  $20$  microns is representative of type 2 AGNs.

The AGN contribution to  $L_{\text{IR}}$  is found to be lower than  $10\%$  except for N-17, the only X-ray source of our sample with broad emission lines, and N-25 which has the highest X-ray luminosity ( $\log(L_X/L_\odot) = 44.4$ ) and exhibits a power-law spectral energy distribution. For these two sources the AGN fraction is found to be larger than  $50\%$ . The current version of CIGALE is unable to fit accurately these SEDs leading to minimum  $\chi^2$  values equal to  $16$  and  $6.4$  for N-17 and N-25 respectively. These two sources will be discarded when the output parameters of the code will be discussed. The case of the other X-ray sources is discussed in section 4.2. Examples of full SED fitting are shown in Fig. 2. The figures for the full sample are available as online material. All the output parameters are estimated through the Bayesian

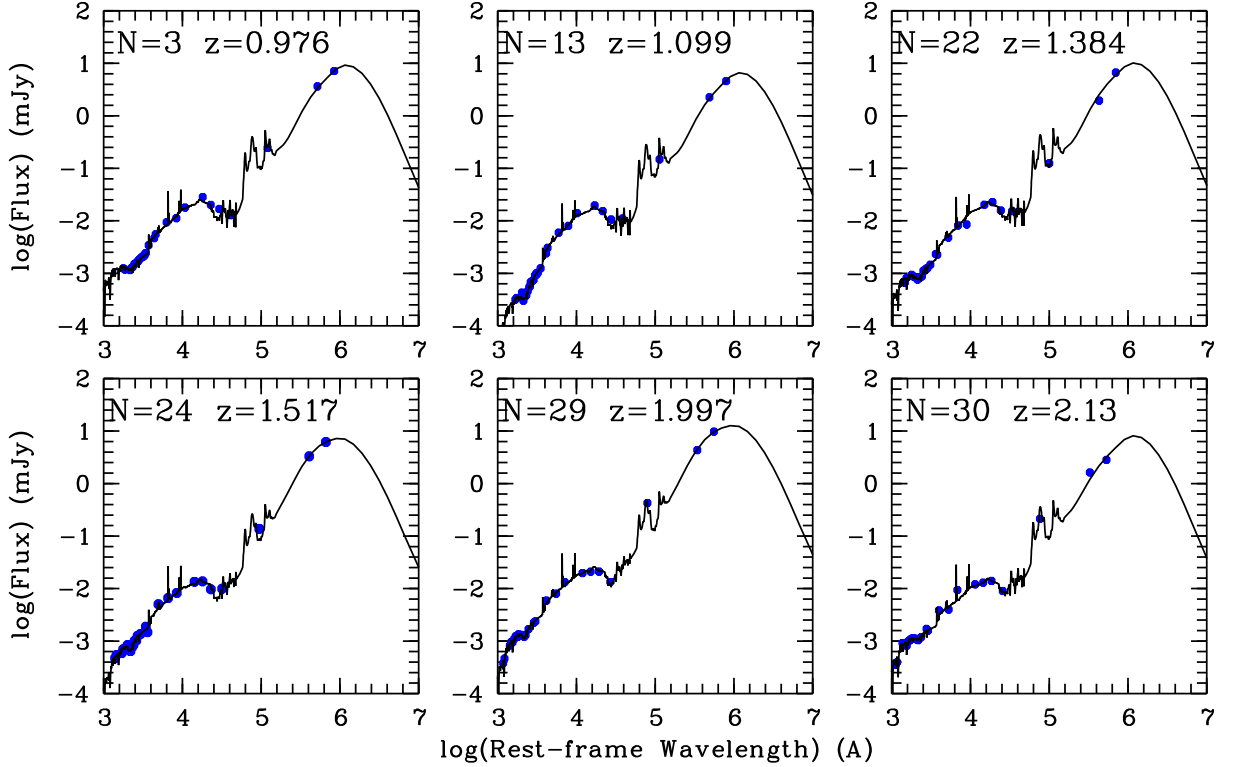


Fig. 2: Examples of SEDs fitted with CIGALE. The best model ( $\chi^2$  minimization) is plotted together with the observed fluxes.

analysis. Results for the total IR luminosity,  $L_{\text{IR}}$ , the dust attenuation at  $1530 \text{ \AA}$ ,  $A_{\text{UV}}$ , and the peak amplitude of the bump,  $E_b$ , are listed in Table 1 together with their errors, also evaluated by a Bayesian calculation (Giovannoli et al., 2010). The range of  $\log(L_{\text{IR}}/L_{\odot})$  is 11.25-12.4 : all the sources are luminous infrared galaxies ( $\log(L_{\text{IR}}/L_{\odot}) > 11$ , LIRG) or ultra luminous infrared galaxies ( $\log(L_{\text{IR}}/L_{\odot}) > 12$ , ULIRG). The mean dust attenuation is found to be quite large with  $\langle A_V \rangle = 0.92 \pm 0.34$  mag and  $\langle A_{\text{UV}} \rangle = 3.09 \pm 1.11$  mag. Such a large dust attenuation is expected for LIRGs and ULIRGs and is favourable to search for the imprint of UV bumps in the spectrum of these galaxies.

## 4. Evidence for a bump at $2175 \text{ \AA}$

### 4.1. Amplitude of the bump from SED fitting with CIGALE

Some examples of SEDs in the UV range are shown in Fig. 3. The figures for the whole sample are available as online material. These few examples show the excellent sampling of the UV SED achieved thanks to the use of medium filters. A dip at  $2175 \text{ \AA}$  is clearly seen in most of the observed SEDs. The best models obtained by the  $\chi^2$  minimization are found to reproduce the

data very well. They all correspond to a bump amplitude larger than 0. The median value of  $E_b$  for the best models is 1.5. In Fig. 4 the Bayesian estimate of  $E_b$  is plotted against the redshift of the sources. All the sources are found to exhibit a bump. The uncertainty given by the Bayesian analysis is quite large but a null amplitude is always excluded at the  $1\sigma$  level. No trend is found either with the redshift or dust luminosity. The mean value  $\langle E_b \rangle = 1.26 \pm 0.30$  corresponds to 35% of the amplitude of the bump in the average extinction curve of the MW and to 76% of that in the LMC2 supershell. (Note that we are dealing with attenuation curve and not extinction ones). Noll et al. (2009a) measured the amplitude of the UV bump in 68 spectra of galaxies with  $1.5 < z < 2.5$  as part of the GMASS survey with a formalism similar to that used in the present work. They detected robustly a UV bump for 24 % of their sample with  $E_b = 0.9 \pm 0.1$  while  $E_b = 0.5 \pm 0.3$  for the remaining 76% of their sample. Our result is marginally consistent with the mean amplitude they measured for their robust detections of a UV bump.

The FWHM of the bump is found to be  $356 \pm 20 \text{ \AA}$ , intermediate between the values found in the MW (and the LMC) and in

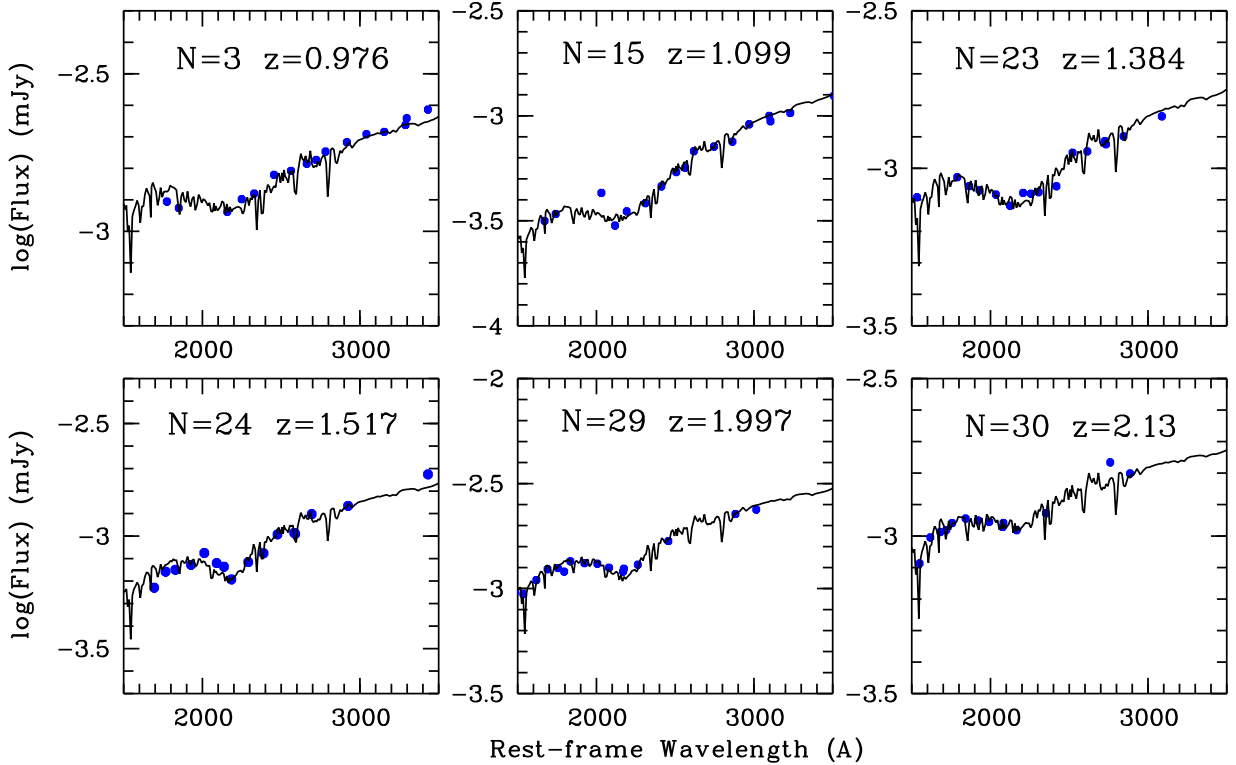


Fig. 3: Spectral energy distributions for  $\lambda < 3500 \text{ \AA}$  for the same objects as in Fig.2, the units, symbols and lines are the same as in Fig.2 except for the scale of the x-axis which is now linear.

galaxies at  $z \sim 2$  (Noll et al., 2009a).

The mean slope of the attenuation curve,  $\delta$ , is found to be  $-0.13 \pm 0.12$ , no trend is found for  $\delta$  as a function of  $E_b$  as shown in Fig.5. Our result is marginally consistent with the Calzetti et al. law which corresponds to  $\delta = 0$ .

#### 4.2. X-ray emitters

Extinction curves of AGN and quasars are found to not display the  $2175 \text{ \AA}$  feature and the wavelength dependence of the extinction in these objects remains controversial between a gray or SMC-like extinction (Li, 2007, and references therein). N17 and N25, two of the seven galaxies in our initial sample classified as X-ray emitters by Cardamone et al. (2010), are discarded because of the bad fitting of their SEDs (see discussion in section 3). The SED fitting process gives amplitudes of the bump for the remaining 5 sources which are different from 0 but in general lower than for non X-ray galaxies (Fig.4). We can quantify this difference: for a Gaussian probability distribution of the parameter  $E_b$ ,  $E_b/err_{E_b} > 2$  corresponds to  $E_b > 0$

with a probability of 95% ( $err_{E_b}$  is the standard deviation of the distribution). Only 2 out of 5 X-ray galaxies fulfill this condition compared to 19 of the 23 non X-ray galaxies (Fig.6). For the first one, N14 (MUSYCID-30046),  $E_b/err_{E_b} = 2.7$ . This galaxy has a high X-ray luminosity,  $\log(L_X/L_\odot) = 44.1$  with a hardness ratio equal to 0.63 (Cardamone et al., 2008). The fit is of average quality with  $\chi^2_{min} = 4.56$  and the presence of a bump is not obvious from a visual inspection of the SED. It is at least partly due to the fact that the best fit model corresponds to a large width of the bump:  $500 \text{ \AA}$ . The second one is N21 (MUSYCID-55660). This galaxy (G02:638) is detected in the hard X-rays with a signal to noise ratio of 2 by Giacconi et al. (2002) only using Sextractor and not with a method based on wavelet transform; Alexander et al. (2003) did not detect this source, so the X-ray detection may be spurious. Its SED shows a clear absorption feature at  $2175 \text{ \AA}$  with  $E_b/err_{E_b} = 5.1$  and the SED fitting is good ( $\chi^2_{min} = 1.71$ ). Given the small number of X-ray sources in our sample as well as the uncertainties inherent to the two sources for which a bump is measured above  $2\sigma$ , we cannot draw any firm conclusion about the presence or not of a

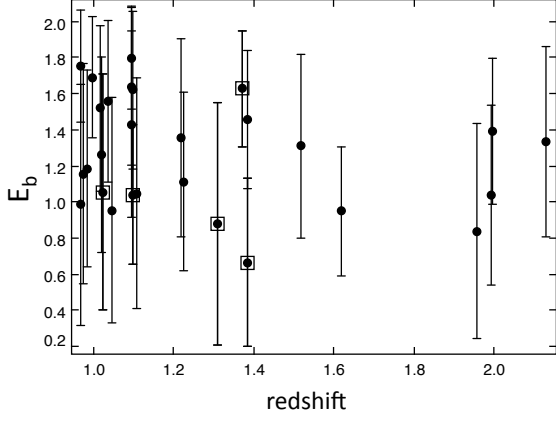


Fig. 4: Amplitude estimated by our Bayesian analysis plotted as a function of redshift of the sources. Galaxies emitting in X-rays are plotted with empty squares. Standard deviations are reported as error bars

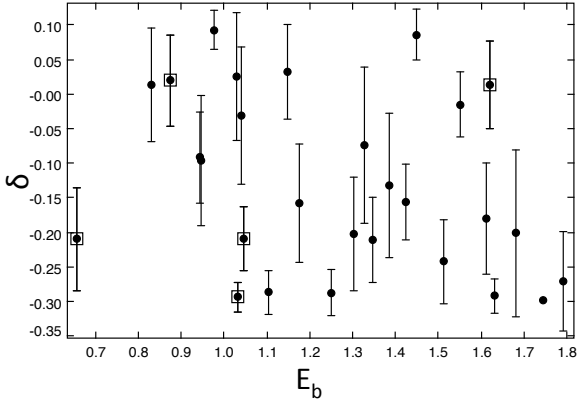


Fig. 5:  $\delta$  versus the amplitude of the bump  $E_b$ . X-ray emitters are encircled with squares

UV bump in the attenuation curve of X-ray galaxies.

The slope of the attenuation curve,  $\delta$ , is found  $\approx 0$  for two X-ray sources and  $\approx -0.2$  for the 3 other ones. Therefore a steep attenuation curve is favoured, not as steep as the SMC extinction curve but excluding a gray extinction which corresponds to positive values of  $\delta$ .

#### 4.3. Average dust attenuation curve

The resulting mean dust attenuation curve obtained for the whole sample is plotted in Fig. 7. All parameters are calculated by a Bayesian analysis. The average dust attenuation curve we obtain can be written:

$$\frac{A(\lambda)}{A_V} = \frac{k'(\lambda) + D_{\lambda_0, \gamma, E_b}(\lambda)}{4.05} \left( \frac{\lambda}{\lambda_V} \right)^{-0.13} \quad (3)$$

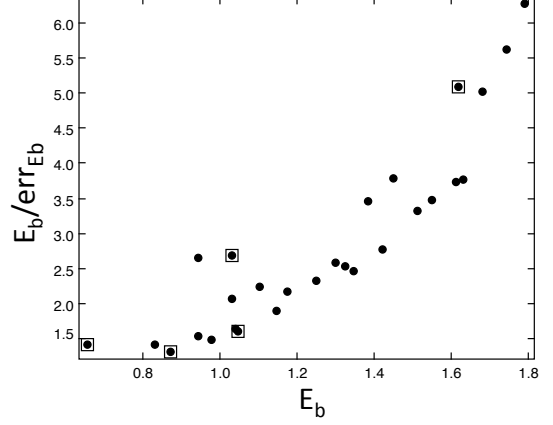


Fig. 6:  $\langle E_b \rangle$ , the mean value of  $E_b$ , divided by its standard deviation  $err_{E_b}$  versus  $\langle E_b \rangle$ .  $E_b/err_{E_b} > 2$  corresponds to  $E_b > 0$  with a probability of 95%. X-ray galaxies are encircled with squares.

where  $\lambda_V = 5500 \text{ \AA}$ ,  $k'(\lambda)$  is given in Calzetti et al. (2000) (Eq.4) and

$$D_{\lambda_0, \gamma, E_b}(\lambda) = \frac{1.26 \times 356^2 \lambda^2}{(\lambda^2 - 2175^2)^2 + \lambda^2 \times 356^2} \quad (4)$$

Strictly speaking this average attenuation curve applies to the young stellar component only (as explained in section 3), the dust attenuation applied to the old component being reduced by a factor 2. In practice, the SEDs of our galaxies appear to be dominated by the young stellar component (modeled as a constant star formation rate over  $\sim 10^8$  years), especially in UV. As a result the global attenuation curve is found to be quite similar to that of the young stellar component alone.

The uncertainty on the average value of  $\delta$  implies quite a large dispersion of the attenuation curve at  $\lambda < 2500 \text{ \AA}$  (Fig. 7) and of the determination of dust attenuation at UV wavelengths. For a visual attenuation  $A_V = 1 \text{ mag}$  the difference between the dust attenuation at  $1500 \text{ \AA}$  obtained by using Eq. 3 ( $\delta = -0.13$ ) or a Calzetti et al. law ( $\delta = 0$ ) reaches 0.5 mag. A value of  $\delta \neq 0$  also implies a change in the value of the effective total obscuration  $R_V = A_V/E_{B-V}$ . Calzetti et al. (2000) obtain  $R_V = 4.05 \pm 0.80$  by comparing the predicted and observed absorbed emission (i.e. by performing an energetic budget). Adopting a value of  $\delta = -0.13$  leads to  $R_V = A_V/E_{B-V} = 3.7$ , still consistent with the value found by Calzetti et al. (2000). The introduction of a bump of moderate amplitude in the dust attenuation curve (Eq. 3) leads to an increase of  $A(\lambda)/A_V$  at  $\approx 2000 \text{ \AA}$  of  $\approx 0.35 \text{ mag}$  as compared to the same curve with  $D_{\lambda_0, \gamma, E_b}(\lambda) = 0$ .

We can compare our average dust attenuation curve to other attenuation curves in the literature. Charlot & Fall (2000) propose a recipe consisting in attenuating the stellar emission by a factor proportional to  $\lambda^{-0.7}$ , and in reducing the normalization of the attenuation for stars older than  $10^7$  years; the resulting effective absorption curve they obtain for a constant star formation rate over  $3 \times 10^8$  years (their Fig. 5) is reported in Fig. 7. A period of  $3 \times 10^8$  years is close to the mean duration of the burst of star formation we obtain for the young stellar population ( $10^8$  years, cf. section 3). Apart from the presence of the bump, not consid-

ered by Charlot & Fall (2000), our mean attenuation curve and that of Charlot & Fall (2000) exhibit similar shapes and steepening for decreasing wavelengths.

Although we are dealing with attenuation and not extinction, we also compare our resulting curve with the extinction curves found in the Milky Way and the Magellanic Clouds. The relative extinctions are compared in Fig. 8. The general shape of the extinction curve of the LMC2 supershell is consistent with our attenuation curve, whereas the MW and SMC extinction curve show flatter and steeper variation, respectively, at short wavelengths.

The exact shape of the extinction curve (slope in the UV range and amplitude of the bump) cannot be constrained with the present data since the attenuation curve we derive strongly depends on the distribution of both stars and dust. Witt & Gordon (2000) show that the shape of the attenuation function also depends on the total amount of dust attenuation. We do not observe any variation of  $E_b$  and  $\delta$  with  $A_{UV}$ : it can be explained by the homogeneity of our sample in terms of dust attenuation associated to the large uncertainties on the determination of these parameters. Radiative transfer models in opaque disks with various configurations of stars and dust (especially in a clumpy medium) are able to reduce the amplitude of the UV bump in the effective attenuation with a dust composition similar to that of the MW or the average LMC, the attenuation curve becoming grayer when the opacity increases (e.g. Witt & Gordon, 2000; Pierini et al., 2004; Inoue et al., 2006; Panuzzo et al., 2007). These models also predict a flattening of the attenuation curve in UV (as an effect of the gray attenuation) as compared to the original extinction curve. The average attenuation curve we deduce increases steeply at short wavelengths: it seems to favour the scenario of a deficiency of bump carriers with respect to the case of MW or average LMC. We will see in section 5.2 that our sources roughly follow the  $A_{UV}$ - $\beta$  relation found by Meurer et al. (1999) for local starbursts which is well explained by a clumpy shell geometry (Witt & Gordon (2000); Calzetti (2001)). Such a dust/star configuration favours the interpretation of a moderate UV bump in the extinction curve itself in agreement with our conclusion (e.g. Witt & Gordon, 2000; Noll et al., 2009a).

## 5. Slope of the UV continuum from broad band photometry and dust attenuation

### 5.1. Determination of the UV slope

#### 5.1.1. Influence of the bump

With the imprint of the UV bump clearly visible in our sample, the assumption of a simple power-law for the entire UV continuum is no longer valid, and its influence in the measured slopes can be quantified. A single power law might be valid if we exclude the spectral region of the bump (Fig.3). Since our fluxes are defined in Jansky we define  $\alpha$  as  $f_\nu \propto \lambda^\alpha$  with  $\alpha = \beta + 2$  where  $\beta$  corresponds to the original definition  $f_\lambda(\text{erg cm}^{-2}\text{s}^{-1}\text{\AA}^{-1}) \propto \lambda^\beta$ . From Fig. 3 it is clear that we can extend the model of a power-law up to 3000  $\text{\AA}$ . Therefore we calculate the slope of the UV continuum in several ways. First we use all the data between 1200 and 3000  $\text{\AA}$ , avoiding the bump range (1975-2375  $\text{\AA}$ ) and perform a linear regression. The resulting value of  $\alpha$  will be taken as our reference  $\alpha_{\text{ref}}$ . Then we define 3 wavelength ranges 1500-2000  $\text{\AA}$  (B1), 1500-2500  $\text{\AA}$  (B2) and 2500-3000  $\text{\AA}$  (B3) which mimic broad band filters and combine two of these bands to estimate  $\alpha$ . The definition of these 3 bands is illustrated in Fig.9 for a galaxy exhibiting a strong bump. B2

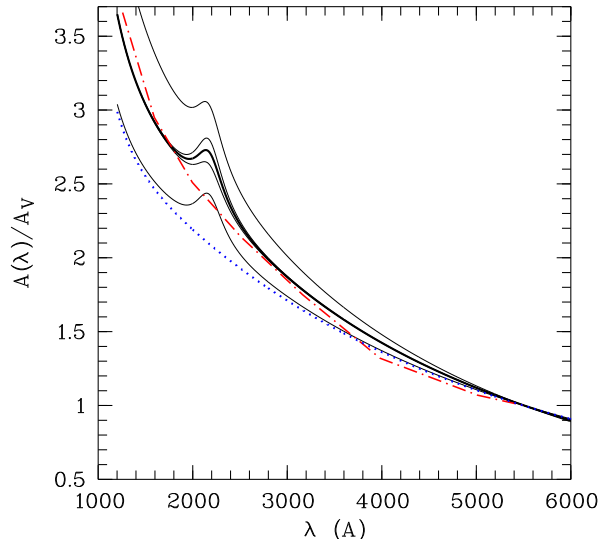


Fig. 7: Average dust attenuation curve. The mean curve found in this work is plotted as a thick line. The thin lines correspond to variations of  $\pm 1\sigma$  of the amplitude of the bump,  $E_b$  and the slope of the continuum  $\delta$ ; see text for details. The Calzetti et al. (2000) attenuation curve (dotted blue line) and the effective absorption curve of Charlot & Fall (2000) for a starburst age of  $3 \cdot 10^8$  years (dot-dashed red line) are shown on the figure for comparison.

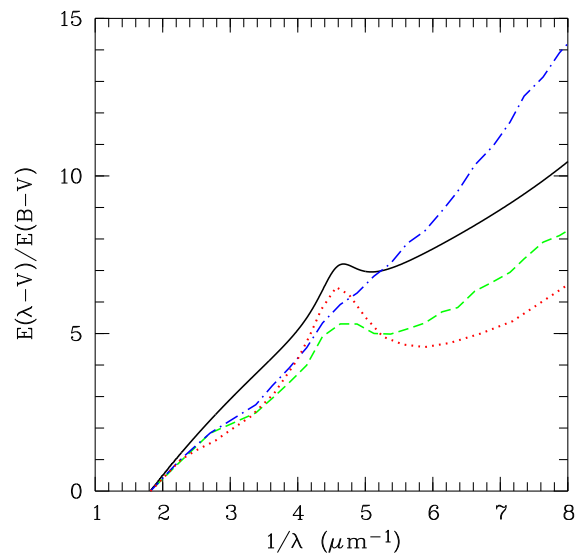


Fig. 8:  $E(\lambda - V)/E(B - V)$ . The mean curve found in this work is plotted as a thick line together with the extinction curve of the MW (red dotted line) from Whittet (2003), LMC2 supershell (green short dashed line) and SMC (blue dot-dashed line) from Gordon et al. (2003).

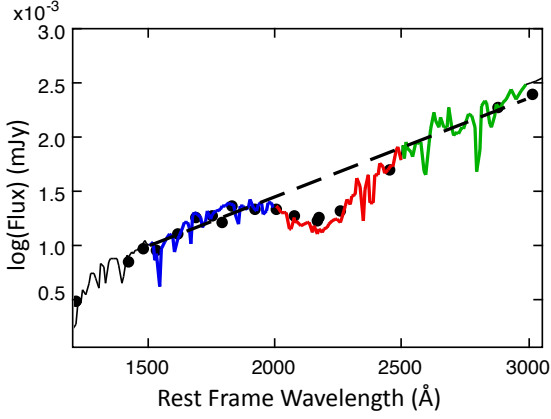


Fig. 9: Definition of 3 bands for ID 2733. The best model found for this galaxy is plotted and the range of wavelengths corresponding to B1, B2 and B3 is in blue, green and red respectively. The black dots are the observed fluxes.

overlaps the bump, therefore we expect some effects when the slope is calculated by considering it. The slopes of the UV continuum are calculated following the prescription of Kong et al. (2004) adapted to our notation:

$$\alpha = \frac{\log(f_{v_i}/f_{v_j})}{\log(\lambda_i/\lambda_j)} \quad (5)$$

where  $f_{v_i}$  and  $f_{v_j}$  are the mean flux densities per unit frequency through the filters  $i$  and  $j$  whose effective wavelengths are  $\lambda_i$  and  $\lambda_j$ . In Fig.10 the  $\alpha$  values obtained by combining B1 and B2 ( $\alpha_{12}$ ), B2 and B3 ( $\alpha_{23}$ ) and B1 and B3 ( $\alpha_{13}$ ) are compared to  $\alpha_{\text{ref}}$  measured on the entire UV SED. As expected  $\alpha_{13}$ , calculated avoiding the bump is found to correlate very well with  $\alpha_{\text{ref}}$  (Fig 10 top panel,  $R = 0.92$ ). The combination of B1-B2 leads to bluer slopes whereas the slopes calculated with B2 and B3 are redder than  $\alpha_{\text{ref}}$ . These effects are expected since the presence of the bump increases the dust attenuation in the B2 band. The amplitude of the shifts are  $\langle \alpha_{12} - \alpha_{\text{ref}} \rangle = -0.46 \pm 0.26$  and  $\langle \alpha_{23} - \alpha_{\text{ref}} \rangle = 0.28 \pm 0.40$  whereas  $\langle \alpha_{13} - \alpha_{\text{ref}} \rangle = -0.09 \pm 0.25$ .

### 5.1.2. GALEX-like UV slope

The FUV and NUV bands of GALEX are commonly used to measure the slope of the UV continuum in the nearby universe (e.g. Seibert et al., 2005). Since the NUV band (1771-2831 Å) (Morrissey et al., 2005) overlaps the UV bump we might expect some underestimation of the slopes.  $\alpha_{\text{GALEX}}$  is an output of CIGALE: the spectral energy distribution of each model generated by the code is integrated in the FUV and NUV (rest-frame) filter bands and  $\alpha_{\text{GALEX}}$  calculated with the above formula. Then the expected value of  $\alpha_{\text{GALEX}}$  for each galaxy of our sample is estimated through a Bayesian calculation (Giovannoli et al., 2010). The correlation between  $\alpha_{\text{GALEX}}$  and  $\alpha_{\text{ref}}$  is very good ( $R = 0.91$ ). As expected  $\alpha_{\text{GALEX}}$  is typically lower (bluer) than  $\alpha_{\text{ref}}$  but the systematic difference remains small with  $\langle \alpha_{\text{GALEX}} - \alpha_{\text{ref}} \rangle = -0.19 \pm 0.24$ . This moderate shift, smaller than the one found considering  $\alpha_{12}$ , is probably due to the wide large bandpass of the NUV filter (1060 Å, (Morrissey et al., 2005)), much wider than the bump itself. Therefore, as long as galaxies exhibit bumps in their attenuation curve similar to those found

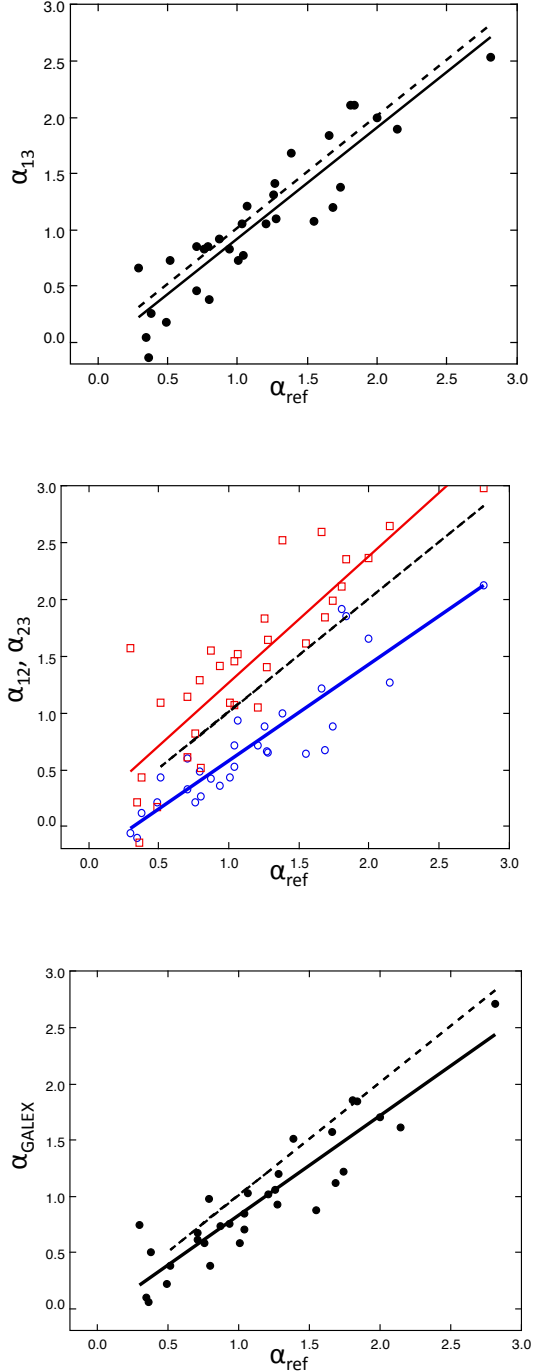


Fig. 10: Various estimates of  $\alpha$  compared to the reference value  $\alpha_{\text{ref}}$  measured on the full SED, top:  $\alpha_{13}$  versus  $\alpha_{\text{ref}}$ ; middle:  $\alpha_{12}$  (blue empty circles) and  $\alpha_{23}$  (red empty squares) versus  $\alpha_{\text{ref}}$ ; bottom:  $\alpha_{\text{GALEX}}$  calculated with the rest-frame FUV and NUV fluxes versus  $\alpha_{\text{ref}}$ . On each figure, the dashed lines represent the 1:1 line, the solid lines are the results of linear regressions.

in this study (1/3 that of the Milky Way), the slopes measured with the GALEX data are found reliable. Burgarella et al. (2005) showed that Milky Way-like bumps have a large influence on the determination of the UV slope with GALEX filters.

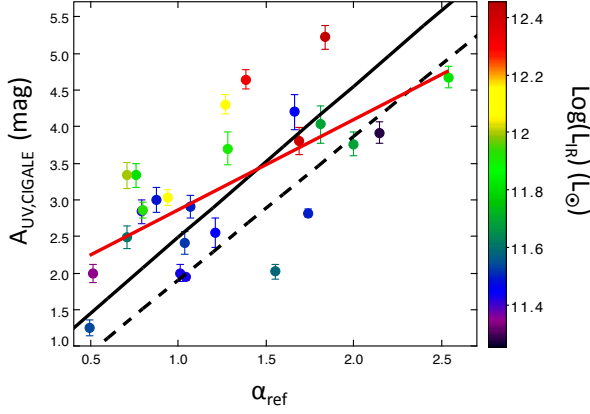


Fig. 11: UV dust attenuations from CIGALE plotted against the slope of the UV continuum calculated with the full SED. The total IR luminosity is colour-coded. The solid and dashed lines correspond to the inner and total relations of Overzier et al. (2011) respectively. The error bars come from CIGALE (Bayesian estimates of the parameters and their associated errors). The red line is the result of the linear regression

### 5.1.3. Impact of photometric errors

It is worth noting that the determination of the UV slope through two broad band filters is very sensitive to photometric errors as well as to the interval between the effective wavelengths of both filters i.e. the factor  $\log(\lambda_i/\lambda_j)$  in Eq.(3). We can re-write Eq.(3) in terms of magnitudes instead of fluxes:

$$\alpha = \beta + 2 = -0.4 \frac{(m_i - m_j)}{\log(\lambda_i/\lambda_j)} \quad (6)$$

Using the FUV and NUV filters of GALEX the relation becomes  $\alpha = -2.22 (m_i - m_j)$  and a typical error of 0.1 mag in FUV and NUV translates to an error of 0.3 on  $\alpha$ . It is obvious from Eq.6 that increasing the wavelength difference between the two filters reduces the uncertainty on the determination of  $\alpha$  and  $\beta$ . For the domain of validity of the power law adopted in this work ( $\lambda < 3000\text{\AA}$ , cf. section 5.1.1), using filters with the largest possible interval between rest-frame wavelength, i.e.  $1300\text{\AA}$  (to avoid the flattening of the attenuation curve for  $\lambda \leq 1200\text{\AA}$  (Leitherer et al., 2002; Buat et al., 2002) and  $3000\text{\AA}$  reduces the error by a factor  $\sim 2$  (this time  $\alpha = -1.11(m_i - m_j)$ ) as compared to the use of GALEX filters.

To summarize, given the uncertainty on the presence and strength of a UV bump in a galaxy, one must avoid as much as possible the region affected by the bump when measuring the UV slope using broad band filters and use filters with effective wavelengths that are as widely separated as possible from each other. If the region of the bump cannot be avoided, the attenuation curve presented in Eq.3 might be used to interpret the data.

### 5.2. Dust attenuation corrections

Meurer et al. (1999) first deduced a relation between  $A_{UV}$  and  $\beta$  for local starbursts, avoiding the bump area on the spectra obtained with IUE. Several calibrations have been proposed since this pioneering work (Calzetti et al., 2000; Seibert et al., 2005;

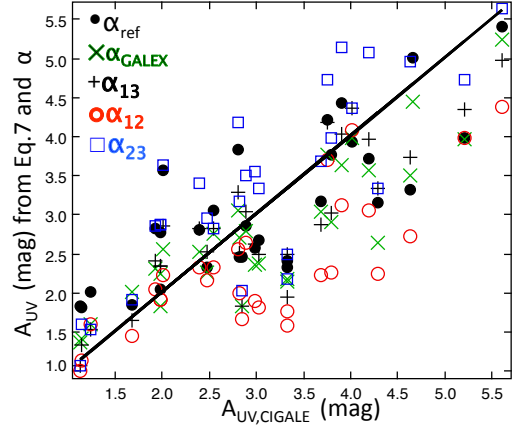


Fig. 12: Comparison of UV dust attenuations: the values of  $A_{UV}$  directly obtained from the SED fitting with CIGALE are plotted on the x-axis and the estimates of  $A_{UV}$  from different UV slopes and Eq. 7 on the y-axis .

Overzier et al., 2011). One issue of the preliminary analyses was that the UV data came from IUE whose aperture sampled only the inner part of the galaxies. Overzier et al. (2011) re-investigate the topic by using GALEX images defining an 'inner' and 'total' relation, the first one based on UV fluxes measured into an IUE-like aperture, the second one corresponding to the total UV fluxes. These relations are:

$$A_{UV} = 4.54 + 2.07\beta = 4.54 + 2.07(\alpha - 2)$$

for the inner relation and

$$A_{UV} = 3.85 + 1.96\beta = 3.85 + 1.96(\alpha - 2)$$

for the total relation. In Fig.11 these relations are compared to the values of  $\alpha_{ref}$  and  $A_{UV,CIGALE}$  (the dust attenuation obtained from the SED fitting process and a Bayesian calculation). Whereas LIRGs seem to follow more or less the local starburst relations, the ULIRGs are found above the local relations which is in agreement with previous studies at low and high redshift (Takeuchi et al., 2010; Howell et al., 2010; Burgarella et al., 2007; Reddy et al., 2008). Buat et al. (2010) performed a selection at  $250\mu\text{m}$  at  $z < 0.3$  and found that their sample (including LIRGs) lie below the local starburst relation. This different behavior is likely to be due to a selection effect biased towards more quiescent galaxies when selected at  $250\mu\text{m}$  than in the mid-IR or around  $60\mu\text{m}$  and to the use of the GALEX colour to measure the UV slope at  $z > 0$ .

A linear regression on the whole sample gives:

$$A_{UV,CIGALE} = 1.46 (\pm 0.21) \alpha_{ref} + 1.50 (\pm 0.29) \quad (7)$$

with a correlation coefficient  $R = 0.79$ . The correlation is rather weak resulting in a large dispersion with a RMS scatter of 0.73 mag. This error directly affects any estimate of  $L_{IR}$  based on relations between  $L_{IR}/L_{UV}$ , a quantity tightly related to  $A_{UV}$  (Buat et al., 2011, and references therein), and the slope of the UV continuum.

We can also compare dust attenuation corrections obtained by applying Eq. 7 to the various estimates of  $\alpha$  defined in section 5.1.1 and 5.1.2. The results are reported in Fig. 12 and compared to the dust attenuation given by CIGALE:  $A_{UV,CIGALE} \cdot A$

large dispersion is found, as a consequence of the loose relation found initially between  $A_{UV}$  and  $\alpha_{ref}$  (Fig 11):  $\langle A_{UV,\alpha_{ref}} - A_{UV,CIGALE} \rangle = -0.005 \pm 0.707$  mag. When using  $\alpha_{13}$  the systematic shift remains moderate  $\langle A_{UV,\alpha_{13}} - A_{UV,CIGALE} \rangle = -0.18 \pm 0.58$  mag.  $\alpha_{GALEX}$ ,  $\alpha_{12}$  and  $\alpha_{23}$  give worse estimates with substantial shifts and large dispersions:  $\langle A_{UV,\alpha_{GALEX}} - A_{UV,CIGALE} \rangle = -0.32 \pm 0.58$  mag,  $\langle A_{UV,\alpha_{12}} - A_{UV,CIGALE} \rangle = -0.73 \pm 0.70$  mag,  $\langle A_{UV,\alpha_{23}} - A_{UV,CIGALE} \rangle = 0.37 \pm 0.71$  mag. Therefore, using UV slopes derived from broad band colours leads to large uncertainties in the derivation of dust attenuation ( $\sim 1$  mag) even if the bump area is avoided and good photometry is available. This is due to the intrinsic dispersion found between the slope of the UV continuum and the amount of dust attenuation. The presence of a bump in one of the filters may add a systematic shift which can reach 0.7 mag for the galaxies of our sample which is likely to be representative of star forming galaxies at redshifts between 1 and 2. These results hold for galaxies with a moderate bump in their dust attenuation curve (35% of the mean amplitude found in the MW) and we expect larger effects for larger bumps.

## 6. Conclusions

We have identified the presence of a UV bump in a sample of galaxies of the CDFS at a redshifts between  $0.9 < z < 2.2$ , selected to be observed in intermediate and broad band optical filters as well as at mid-and far-IR wavelengths by *Spitzer* and *Herschel*. This study demonstrates the capabilities of intermediate-band photometry to give details on SED of galaxies, and to derive physical properties.

The average dust attenuation curve we deduce is well described by a modified Calzetti et al. law slightly steeper than the original one and with a UV bump at  $2175 \text{ \AA}$  whose amplitude is  $\sim 35\%$  of the MW one. We propose an analytical expression of the average attenuation curve which can be used to correct the SEDs of galaxies for dust attenuation. The moderate amplitude of the bump together with the substantial slope of our average attenuation curve in the UV argue for a deficit of UV bump carriers in our sample galaxies as compared to the MW.

Our sample contains seven X-ray galaxies. Five of them are reasonably fitted: a steep attenuation curve is favoured excluding a gray extinction. The sample is too small to draw any firm conclusion about the presence of a UV bump. In any case the amplitude of the bump, if any, is smaller than that found for non X-ray galaxies.

The presence of a bump in the mean dust attenuation curve has implications for the derivation of the slope of the UV (rest-frame) continuum of galaxies from broad band data alone. The power law modeling of the UV spectral distribution of our galaxies can be extended up to  $3000 \text{ \AA}$  but the bump area must be avoided. When a broad band filter overlaps the bump, despite its moderate amplitude, the error on the determination of the slope may reach  $\sim 0.5$ . The use of GALEX filters leads to an underestimation of the slope of only 0.2, even if the NUV filter overlaps the bump. This is likely to be due to the very large bandpass of this filter. However, the proximity of the two central wavelengths of the GALEX filters implies a large uncertainty in the determination of the slope. It is stressed that a larger wavelength baseline would give a better measure.

Dust attenuation estimated with UV slopes, even when the latter are reliable, remains uncertain, with an RMS error of 0.7 mag.

*Acknowledgements.* This work is partially supported by the French National Agency for research (ANR-09-BLAN-0224). PACS has been developed by a consortium of institutes led by MPE (Germany) and including UVIE (Austria); KU Leuven, CSL, IMEC (Belgium); CEA, LAM (France); MPIA (Germany); INAF/IFSI/OAA/OAP/OAT, LENS, SISSA (Italy); IAC (Spain). This development has been supported by the funding agencies BMVIT (Austria), ESA-PRODEX (Belgium), CEA/CNES (France), DLR (Germany), ASI/INAF (Italy), and CICYT/MCYT (Spain).

## References

- Alexander, D.M. et al. 2003, AJ, 126, 539  
 Buat, V., Burgarella, D., Deharveng, J.M., Kunth, D. 2002, A&A, 393, 33  
 Buat, V., Giovannoli, E., Burgarella, D. et al. 2010, MNRAS 409, L1  
 Buat, V., Giovannoli, E., Takeuchi, T.T. et al. 2011, A&A, 529, 22  
 Burgarella, D., Buat V., Iglesias-Páramo, J. 2005, MNRAS, 360, 1413  
 Burgarella, D., Le Flocc'h, E., Takeuchi, T. T., Huang, J. S., Buat, V., Rieke, G. H., Tyler, K. D. 2007, MNRAS, 380, 986  
 Calzetti, D., Kinney, A.L., Storchi-Bergmann, T. 1994, ApJ 429, 582  
 Calzetti, D., Armus, L., Bohlin, R. C. et al. 2000, ApJ, 533, 682  
 Calzetti, D., 2001, PASP, 113, 1449  
 Charlot, S., Fall, S.M. 2000, ApJ 539, 718  
 Cardamone, C.N., Urry, P.G., Damen, M. et al. 2008, ApJ, 680, 130  
 Cardamone, C.N., van Dokkum, P.G., Urry, C. M. et al. 2010, ApJSS, 189, 270  
 Cartledge, S.I.B., Clayton, G.C., Gordon, K.D. et al. 2005, ApJ 630, 355  
 Conroy, C. 2010, MNRAS, 404, 247  
 Conroy, C., Schiminovich, D., Blanton, M.R. 2010, ApJ, 718, 184  
 Dale, D. A. , Helou, G. 2002, ApJ, 576, 159  
 Daddi E., Alexander, D.L., Dickinson, M. et al. 2007, ApJ, 670, 156  
 Dickinson, M., Giavalisco, M. and the GOODS team, 2003, in "The Mass of Galaxies at Low and High Redshift", eds. R. Bender and Alvio Renzini, Springer, p. 324.  
 Draine, B.T. 1989, in "Interstellar Dust", proceeding of the 135th Symposium of the IAU, eds. L. J. Allamandola and G.G.M. Tielens, p. 313  
 Elbaz, D., Daddi, E. , Le Borgne, D. et al. 2007, A&A, 468, 33  
 Elbaz, D. , Hwang, H.S., Magnelli, B. et al. 2010, A&A, 518, L29  
 Elbaz, D. et al. 2011, arXiv:1105.2537  
 Fitzpatrick, E.L., Massa, D. 1990, ApJS, 72, 163  
 Fitzpatrick, E.L., Massa, D. 2007, ApJ, 663, 320  
 Fritz, J., Franceschini, A., Hatziminaoglou, E. 2006, MNRAS 366, 767  
 Giacconi, R., Zirm, A., Wang, J. et al. 2002, ApJSS 139, 369  
 Giovannoli, E., Buat, V., Noll, S., Burgarella, D., Magnelli, B. 2010, A&A 525, 150  
 Gordon K.D., Clayton, G.C., Misselt, K.A., Landolt, A.U., Wolff, M.J. 2003, ApJ, 594, 279  
 Howell J. H., Armus, L., Mazzarella, J.M. et al. 2010, ApJ, 715, 572  
 Inoue, A., Buat, V., Burgarella, D., Panuzzo, P., Takeuchi, T.T., Iglesias-Paramo, J. 2006, MNRAS, 370, 380  
 Ilbert, O., Capak, P., Salvato, M. et al. 2009, ApJ, 690, 1236  
 Johnson, B.D., Schiminovich, D., Seibert, M. et al. 2007, ApJ 173, 377  
 Johnson, B.D., Schiminovich, D., Seibert, M. et al. 2007, ApJ 173, 392  
 Kong, X. Charlot, S., Brinchmann, J., Fall, S. M. 2004, MNRAS, 349, 769  
 Kriek, M., van Dokkum, P.G., Whitaker, K.E., Labbe? I., Franx, M., Brammer, G.B. 2011 arXiv:1103.0279  
 Leitherer, C., Li, I.H., Calzetti, D., Heckman, T.M. 2002, ApJS 140, 303  
 Liang, S.L., Li, A 2009, ApJ690, L56  
 Liang, S.L., Li, A 2010, ApJ710, 648  
 Li, A. 2007, in "The Central Engine of Active Galactic Nuclei", ASP Conference Series, vol 373, eds. L. C. Ho and J-M Wang, p. 561  
 Li, A., Draine, .B.T. 2002, ApJ, 576, 762  
 Meurer, G. R., Heckman, T. M., & Calzetti, D. 1999, ApJ, 521, 64  
 Melbourne, J., Koo, D., Le Flocc'h, E. 2005, ApJ, 625 L65  
 Morrissey, P., Schiminovich, D., Barlow, T. A. et al. 2005, ApJ, 619, L7  
 Mullaney, J.R., Alexander, D.M., Goulding, A.D., Hickox, R.C., 2011, MNRAS, 414, 1082  
 Noll, S, Pierini, D. 2005, A&A 137, 155  
 Noll, S, Pierini, D., Pannella, M., Savaglio, S. 2007, A&A 472, 455  
 Noll, S., Pierini, D., Cimatti, A. et al. 2009a, A&A 499, 69  
 Noll S., Burgarella D., Giovannoli E. et al. 2009b, A&A, 507, 1793  
 Overzier, R., Heckman, T.M., Wang, J. et al. 2011, ApJ, 726, L7  
 Panuzzo P., Granato G. L., Buat V., Inoue A. K., Silva L., Iglesias-Páramo J., Bressan A., 2007, MNRAS, 375, 640  
 Pierini, D., Gordon, K.D., Witt, A.N., Madsen, G.J. 2004, ApJ, 617, 1022  
 Pilbratt, G., Riedinger, J. R., Passvogel, T., et al. 2010, A&A 518, L1  
 Poglitich, A., Waelkens, C., Geis, N. et al. 2010, A&A 518, L2  
 Reddy, N. A., Steidel, C. C., Pettini, M. et al. 2008, ApJ, 692, 778  
 Seibert, M., Martin, D. C., Heckman, T.M. et al. 2005, ApJ 619, L55

- Siebenmorgen, R., Freudling, W., Krügel, E., Haas, M. 2004, A&A, 421, 129  
Takeuchi T. T., Buat V., Heinis S. et al. 2010, A&A, 514, A4  
Vijh, U., Witt, A.N., Gordon, K.D. 2003, ApJ 587, 533  
Wijesinghe, D.B., Hopkins, A.M. Sharp, R. et al. 2011, MNRAS, 410, 2291  
Whittet, D.C.B. 2003, Dust in the Galactic environment, series in Astronomy  
and Astrophysics (Institute of Physics Publishing)  
Witt, A. N., Gordon, K.D. 2000, ApJ, 528, 799  
Xiang, F.Y, Li, A., Zhng, J.X. 2011, ApJ, 733, 91  
Zafar, T. Watson, D., Fynbo, J.P.U., Malesani, D., Jakobson, P., de Ugarte  
Postigo, A. 2011, arXiv:1102.1469

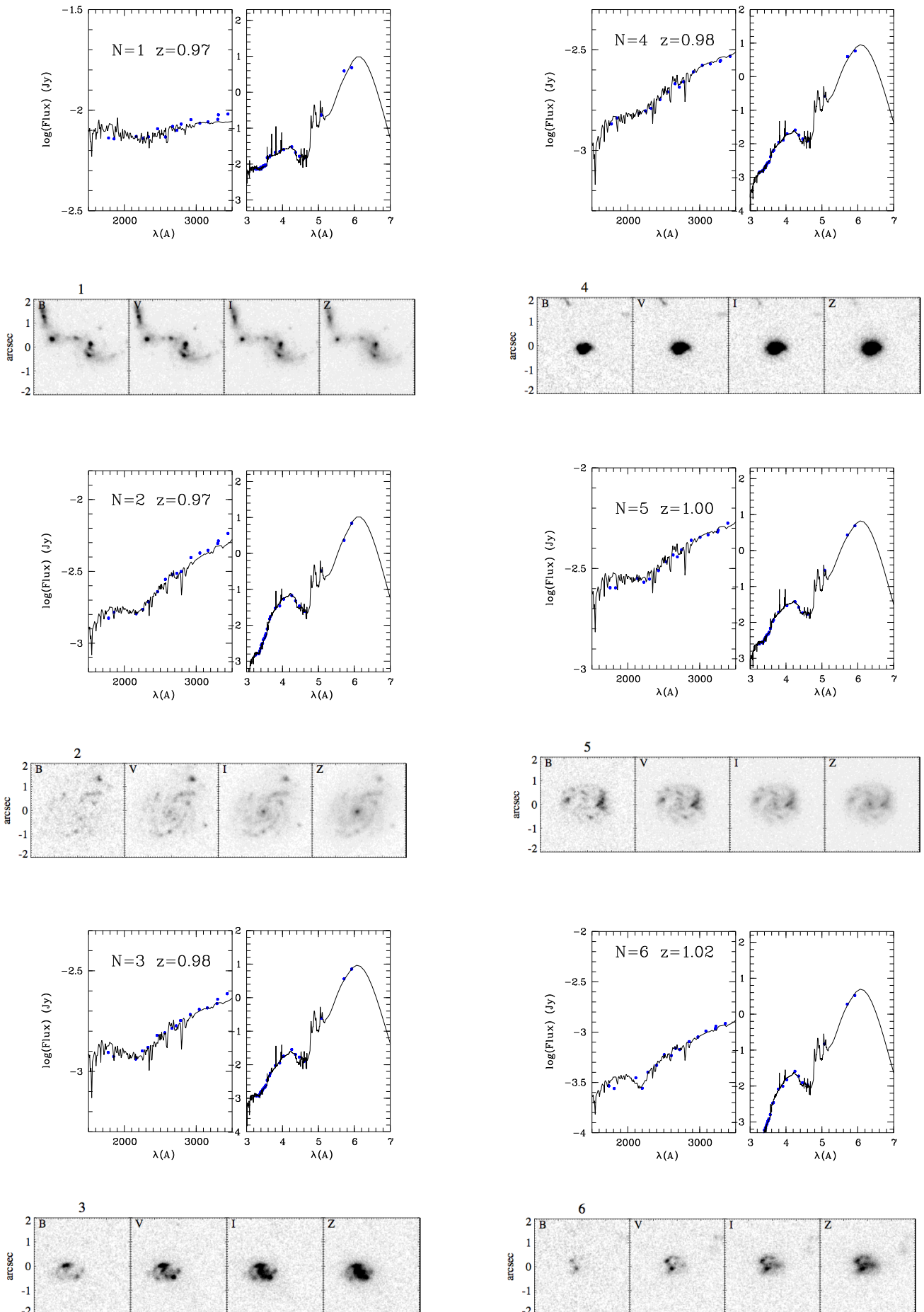


Fig. 1: cont'd

Fig. 1: Spectral energy distributions for the full sample and HST images obtained from the GOODS cutout service V0.2. The best fit is represented with a solid line. The rest-frame wavelength is plotted on the x-axis and the fluxes in Jy on the y-axis.

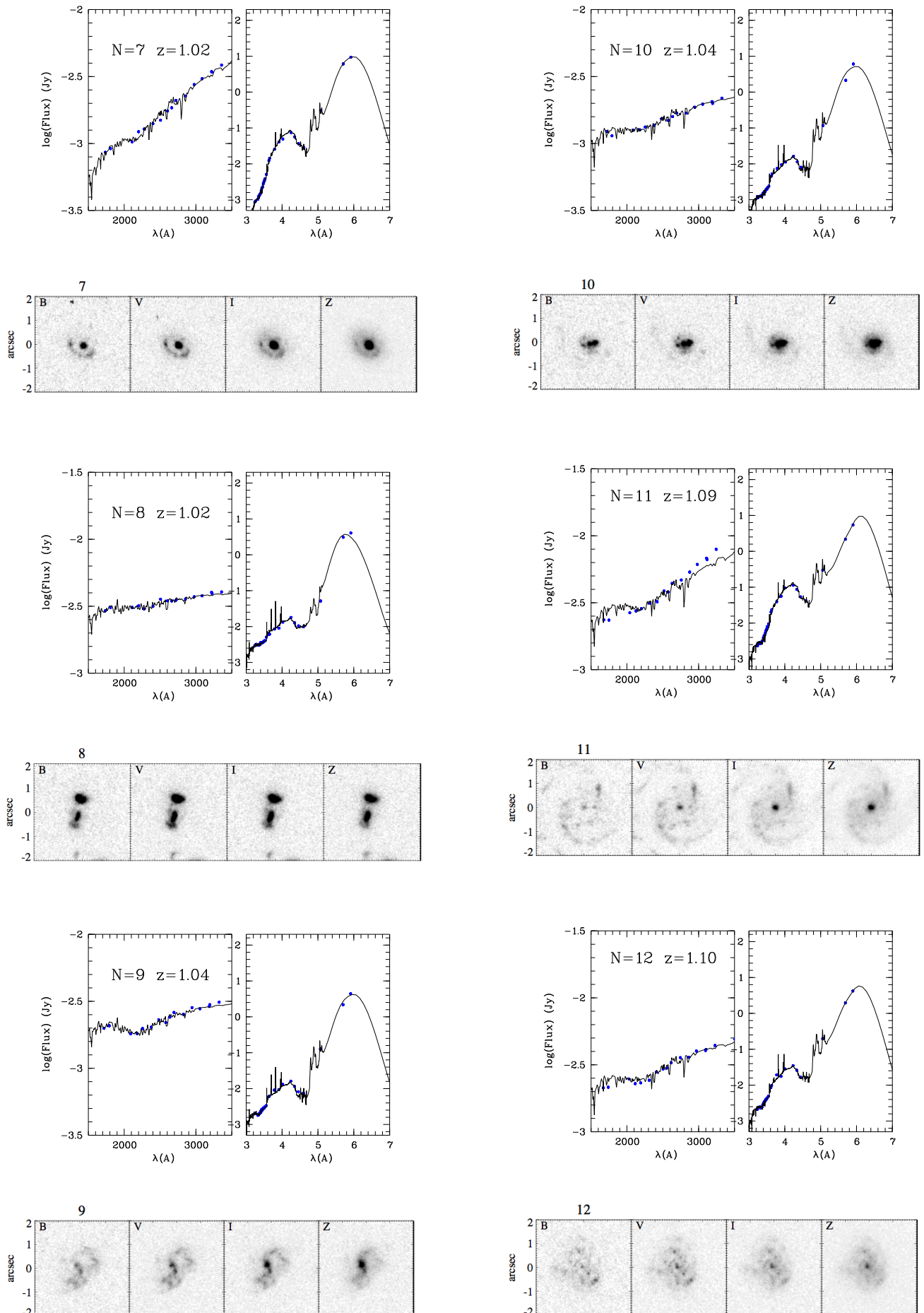


Fig. 1: cont'd

Fig. 1: cont'd

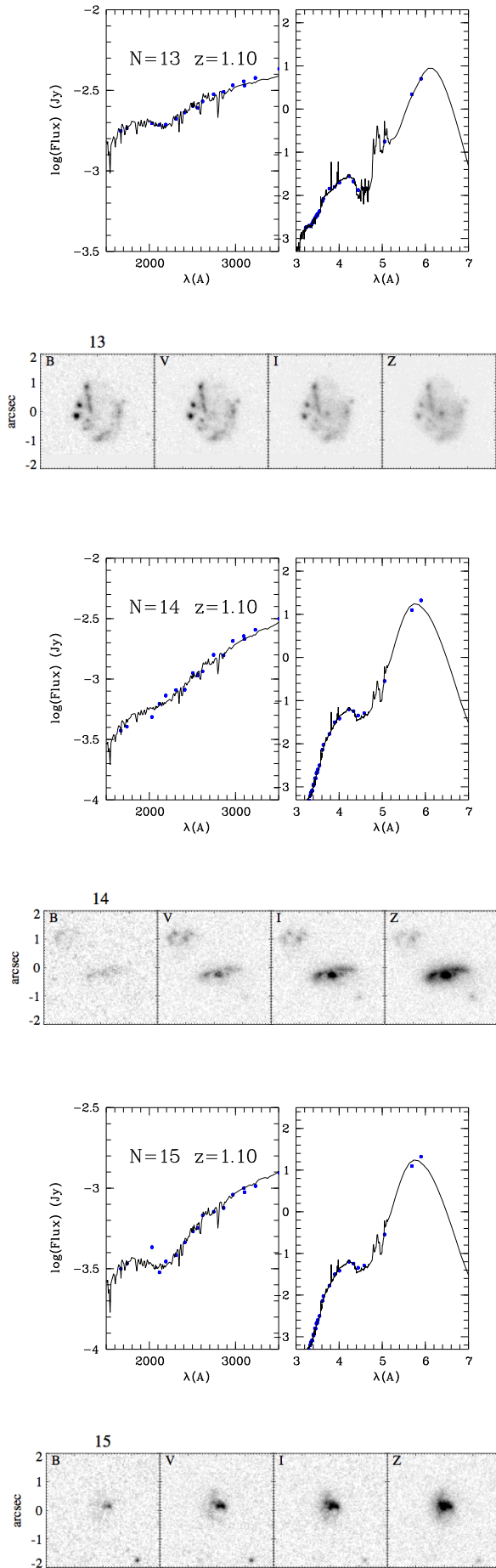


Fig. 1: cont'd

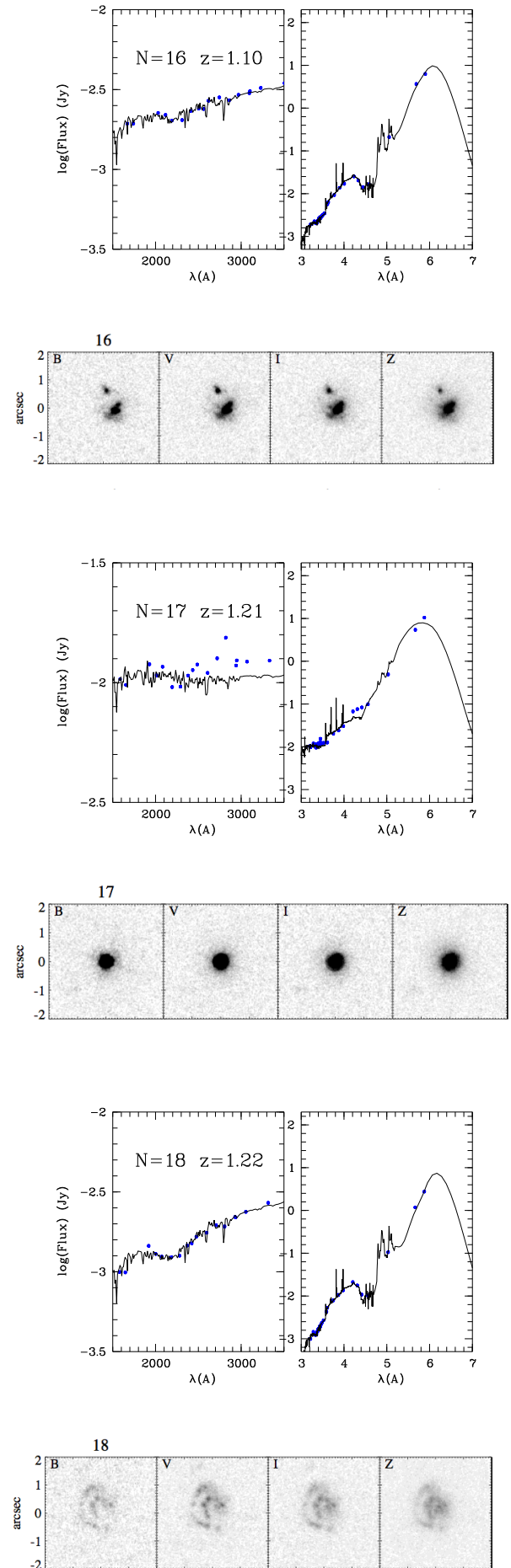


Fig. 1: cont'd

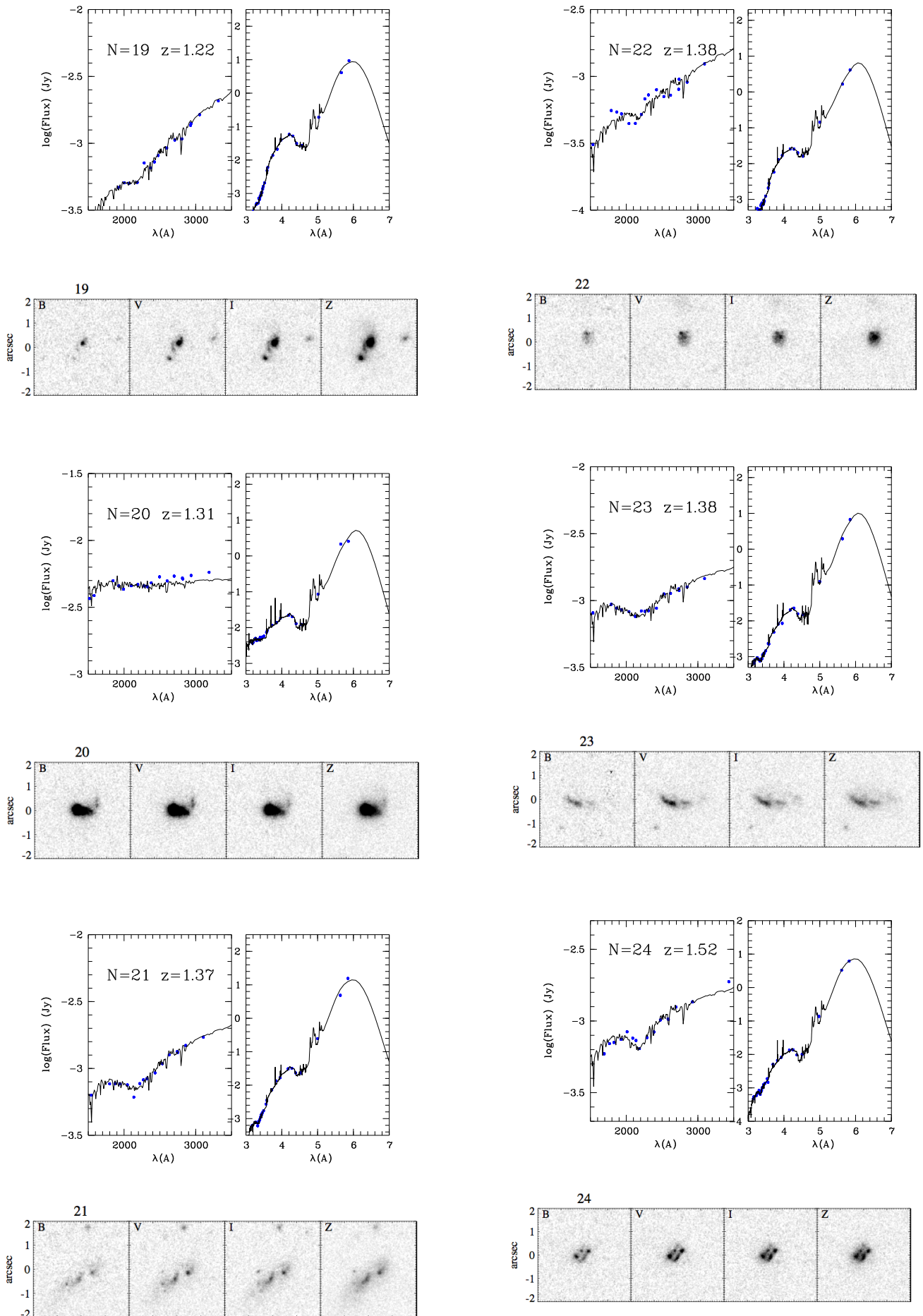


Fig. 1: cont'd

Fig. 1: cont'd

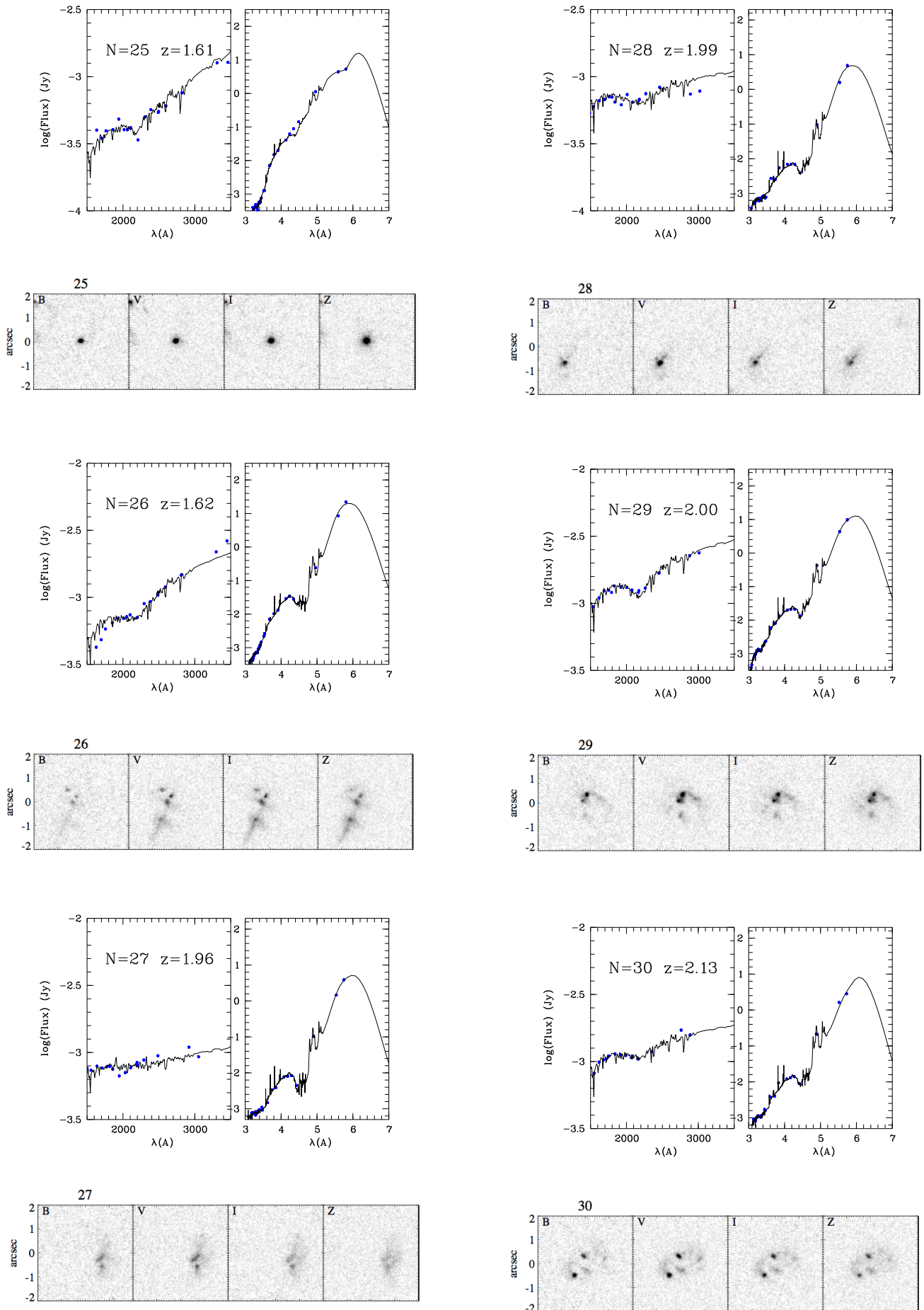


Fig. 1: cont'd

Fig. 1: cont'd